Plasmonics (2018) 13:1165–1170
DOI 10.1007/s11468-017-0617-y

A Novel Diamond Ring Fiber-Based Surface Plasmon Resonance Sensor

Wee Lit Ng[1] · Ahmmed A. Rifat[2] · Wei Ru Wong[1] · G. A. Mahdiraji[3,4] · F. R. Mahamd Adikan[1,4]

Received: 21 January 2017 / Accepted: 9 May 2017 / Published online: 21 May 2017

Abstract We propose a highly sensitive novel diamond ring fiber (DRF)-based surface plasmon resonance (SPR) sensor for refractive index sensing. Chemically active plasmonic material (gold) layer is coated inside the large cavity of DRF, and the analyte is infiltrated directly through the fiber instead of selective infiltration. The light guiding properties and sensing performances are numerically investigated using the finite element method (FEM). The proposed sensor shows a maximum wavelength and amplitude interrogation sensitivity of 6000 nm/RIU and 508 RIU^{-1}, respectively, over the refractive index range of 1.33–1.39. Additionally, it also shows a sensor resolution of 1.67×10^{-5} and 1.97×10^{-5} RIU by following the wavelength and amplitude interrogation methods, respectively. The proposed diamond ring fiber has been fabricated following the standard stack-and-draw method to show the feasibility of the proposed sensor. Due to fabrication feasibility and promising results, the proposed DRF SPR sensor can be an effective tool in biochemical and biological analyte detection.

Keywords Surface plasmon resonance · Fiber optics · Optical fiber sensor

✉ Wee Lit Ng
princeng89@gmail.com

[1] Integrated Lightwave Research Group, Department of Electrical Engineering, Faculty of Engineering, University of Malaya, 50603 Kuala Lumpur, Malaysia

[2] School of Engineering and Information Technology, University of New South Wales, Canberra, ACT 2610, Australia

[3] School of Engineering, Taylor's University, 47500 Subang Jaya, Selangor, Malaysia

[4] Flexilicate Sdn. Bhd., University of Malaya, 50603 Kuala Lumpur, Malaysia

Introduction

Surface plasmon resonance (SPR) sensor attracts much attention since last few decades due to its high sensitive nature and broad range of sensing applications such as medical diagnostics, biomolecular analyte detection, and antibody-antigen interaction [1–3]. SPR refers to the resonant oscillation of free electrons of metal and electromagnetic fields due to incident light in a meal-dielectric interface.

In 1983, Liedberg et al. [4] reported the first prism SPR technique for biosensing and gas detection. The prism-based SPR sensor does give robust performance. However, its bulky structural configuration resulting from the optical and mechanical components is not convenient for remote sensing [3, 5]. To overcome the prism SPR sensor limitations, photonic crystal fiber (PCF)-based SPR sensors have been proposed. PCF is compact and miniaturize in size which benefits the SPR sensing applications. Besides the SPR sensing, fiber or waveguide-based refractive index (RI) sensing techniques such as fiber Bragg grating (FBG), modal interferometer, long period fiber grating (LPFG), and micro-ring resonator-based sensing have been proposed [6–10]. However, only a very narrow wavelength shift will be shown by these sensors against the changes in analyte RI. On the contrary, SPR sensor provides high sensitivity by showing large resonance wavelength shift even against a very small RI difference. The first optical fiber SPR sensor has been demonstrated by Jorgenson [11] in 1993. Following that, various PCF SPR sensors have been proposed to improve the SPR sensing performance. In 2006, Hassani et al. reported the microstructured optical fiber-based SPR sensor for the first time [12]. Recently, PCF SPR

sensors with inside metal coating and selective liquid infiltration into the air holes have been studied [13–18]. However, their practical implementation are very challenging, especially the process to infiltrate liquid selectively into small air holes. To overcome the limitations, D-shaped PCF SPR sensors have been introduced [19, 20], where metallic layer and analyte layer are directly applied onto the flat top surface of D-shaped PCF. Nonetheless, this requires extra effort on accurate polishing remove the predetermined portion of PCF. In other studies, outside metal deposition and sensing layer formation have been proposed with irregular PCF structures [21–24]. Outside sensing layer formation paves a simple sensing process. However, due to the irregular geometry of the microstructure optical fiber, fabrication of such fiber is challenging. Also, structures with outer coating are environmentally sensitive and require extra precaution in handling. Experimental study of PCF-based SPR sensors are yet to be explored in a large scale due to the complexity of reported fiber structures.

In this paper, a new type of microstructured fiber which is referred to as DRF-based SPR sensor has been proposed [25]. This fiber is fabricated using the conventional stack-and-draw fiber drawing method. DRF provides relatively large cavities as compared to those reported PCFs which eases the metal coating process. Due to the large cavity of DRF, homogeneous metal coating onto the surface of the cavity can be done by high pressure chemical vapor deposition (CVD) technique [26, 27]. Apart from the advantage of having large cavities, DRF SPR sensor does not require selective infiltration of analyte. The proposed DRF SPR sensor shows high sensitivity in both wavelength and amplitude interrogation methods. Using the proposed sensor, unknown analytes could be detected following the flow cell analyte continuing process [28].

Structural Design and Theoretical Modeling

Cross-sectional view of the proposed DRF SPR sensor is shown in Fig. 1a. DRF is an all-silica fiber which is having a ring capillary with the thickness, $t_r = 0.94$ μm, to support the core in the middle along the fiber. The core size of the fiber, d_{core}, is measuring at 3.23 μm. Gold metal layer with the thickness, $t_{\text{gold}} = 50$ nm, is coated on the inner wall of the ring capillary. Analyte is infiltrated into both of the DRF's cavities, small one with the diameter $d_1 = 21.36$ μm and the large one with the diameter $d_2 = 46$ μm. The refractive index of silica, n_{silica}, is obtained according to the operating wavelength, λ following Sellmeier equation [29]. The dielectric constant of gold is determined by using the Drude-Lorentz model [30] with the equation as shown in Eq. (1):

$$\varepsilon_{\text{Au}} = \varepsilon_{\infty} - \frac{\omega_D^2}{\omega(\omega + j\gamma_D)} - \frac{\Delta\varepsilon.\Omega_L^2}{\left(\omega^2 - \Omega_L^2\right) + j\Gamma_L\omega} \quad (1)$$

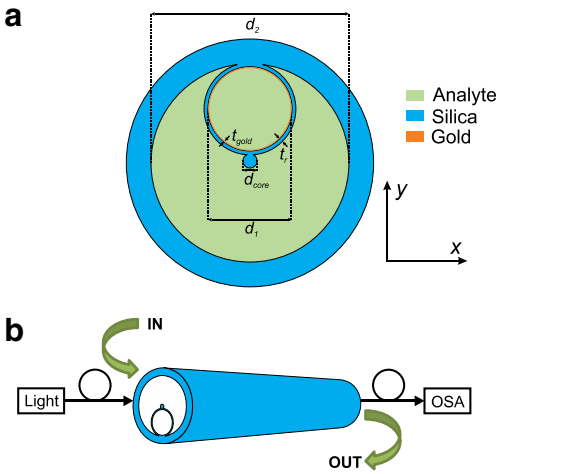

Fig. 1 **a** Cross-section of the proposed sensor. **b** Schematic diagram of the experimental setup

where ε_{Au} is the permittivity of the gold material and ε_{∞} is the permittivity at high frequency with the value of 5.9673. ω is the angular frequency which can be expressed as $\omega = 2\pi c/\lambda$ where c is the velocity of light in vacuum. ω_D is the plasma frequency in which $\omega_D/2\pi = 2113.6$ THz whereas γ_D is the damping frequency in which $\gamma_D/2\pi = 15.92$ THz. The value of the weighting factor $\Delta\varepsilon$ is 1.09. Spectral width and oscillator strength of the Lorentz oscillators are expressed as $\Gamma_L/2\pi = 104.86$ and $\Omega_L/2\pi = 650.07$ THz, respectively.

Commercially available COMSOL MULTIPHYSICS™ software utilizing finite element method (FEM) is used to investigate the light guiding properties and sensing performances of the proposed sensor. The circular perfectly matched layer (PML) boundary condition has been considered to absorb the scattered light towards the surface.

The possible experiment setup for DRF SPR sensor is demonstrated in Fig. 1b. Supercontinuum laser source could be used to launch the incident light into the sensor via single-mode polarization-maintaining fiber (PMF) and aligned to the sensor through butt-coupling. The output from the sensor will be analyzed by the optical spectrum analyzer (OSA).

Results and Discussion of the Proposed DRF SPR Sensor

The fabrication of the proposed DRF is based on conventional stack-and-draw method [31] where two glass tubes have been selected for stacking the preform of DRF, first one with inner to outer diameter of 17.5 mm/25 mm, used as the jacket tube and second one measuring 18 mm/20 mm, to be pulled into capillaries with smaller outer diameter of 8.12 mm. One of those capillaries was inserted into the jacket tube. Its position was fixed by two pieces of short length capillaries at both ends. A silica rod was then inserted into the central space formed by the stacked capillaries. DRF preform was annealed

at 1800 °C to join the surface of the long capillary and silica rod. The preform was then pulled into cane measuring 1 mm in diameter at the temperature of 1930 °C. The drawing speed of 1.6 m/min was determined based on the conservation of mass equation. Pressure was carefully applied into the long capillary to ensure the position of silica rod at the middle of the cane. The structure of the cane was checked under microscope throughout the whole cane pulling process. First few meters of the cane are those with three-ring structure resulting from the aforementioned supporting short capillaries. The canes were collected after the one-ring DRF structure was produced. The cane was then inserted into two consecutive larger capillaries to form a double-jacketed cane. With drawing speed of around 1.5 m/min and temperature of around 1850 °C, it was drawn into DRF measuring 125 μm in diameter. The diameter of the DRF was chosen to be 125 μm for easier splicing with the standard single-mode fiber. The scanning electron microscope (SEM) image of the fabricated DRF is shown in Fig. 2. The fabricated DRF is the same as the desired structure with measured parameters of d_{core} = 6.68, d_1 = 35.1, d_2 = 90.2, and t_r = 2.51 μm.

The SEM image of the fabricated sample was imported into COMSOL MULTIPHYSICS™ software and a thin gold layer (50 nm) was applied onto the inner surface of the round cavity. The cavities were filled with analyte of refractive index (RI) n_a and the structure is ready to be analyzed theoretically as the proposed DRF SPR sensor.

DRF SPR sensor is working based on the principle of interaction between evanescent field and the gold layer. Evanescent field produces from the core-guided light penetrates into the air cavity where the gold layer is coated. Resonance will be occurred while the real part of n_{eff} of the core-guided mode and surface plasmon polaritons (SPP) mode is mathematically same. Core-guided mode is coupled to the SPP mode at a resonance condition which is called the phase-matching point and produces a sharp loss peak.

Figure 3 shows the phase-matching condition of the proposed sensor. As shown in Fig. 3a, the sensor shows higher resonance loss peak using y-polarized fundamental mode as compared to that of x-polarized fundamental mode. Figures 3b, c show the y-polarized core mode and x-polarized core mode, respectively. Obviously, the y-component electric field is stronger in the sensing layer due to the fact that it is refracted towards the metal surface. Hence, later in this work, y-polarized light is considered. Figure 3d shows the SPP mode on the surface of the metal. With the analyte RI of 1.33, phase matching was found at λ = 620 nm where the dispersion relations of core-guided mode and SPP mode intersects and resonance peak loss occurs. The confinement loss was calculated by following the equation $\alpha(dB/cm) = 8.686 \times (2\pi/\lambda)\mathrm{Im}(n_{eff}) \times 10^4$ [18], where $Im(n_{eff})$ is the imaginary part of the effective mode index and λ is expressed in the unit of micrometer. Largest energy is transferred to SPP mode from the core-guided mode at this phase-matching point. Both of the modes are strongly coupled as shown in Fig. 3e.

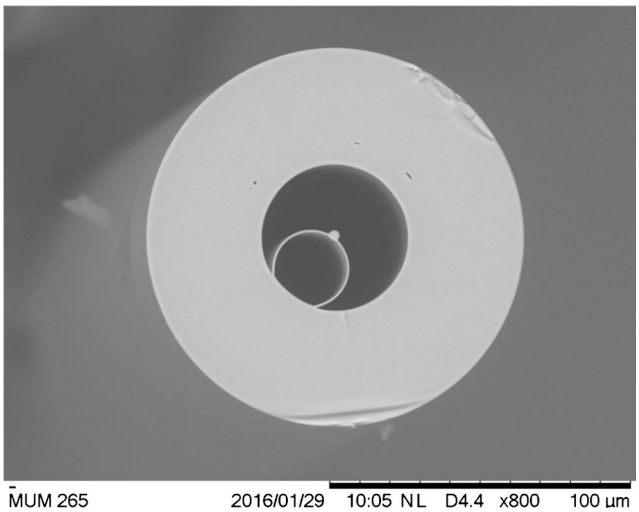

Fig. 2 SEM image of the fabricated DRF

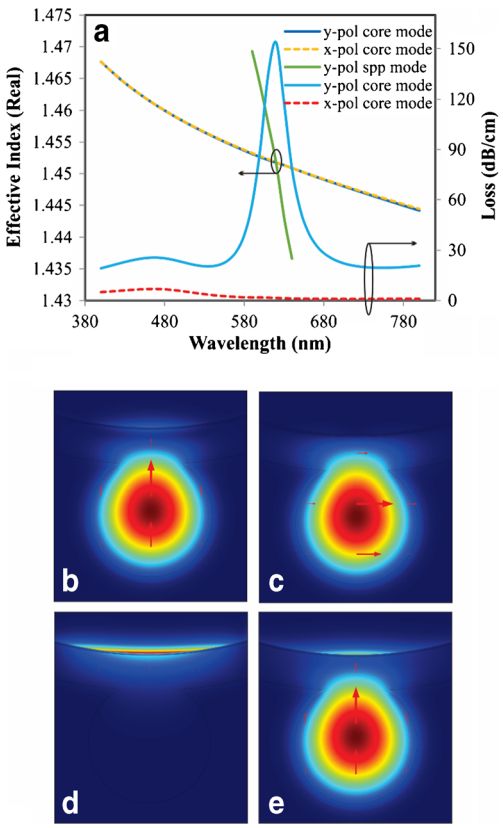

Fig. 3 **a** Dispersion relations of core-guided modes and SPP mode with analyte RI of 1.33. Electric field distributions of the **b** y-polarized core mode, **c** x-polarized core mode, **d** y-polarized plasmon mode at λ = 580 nm, and **e** y-polarized core mode at λ = 620 nm (phase-matching point)

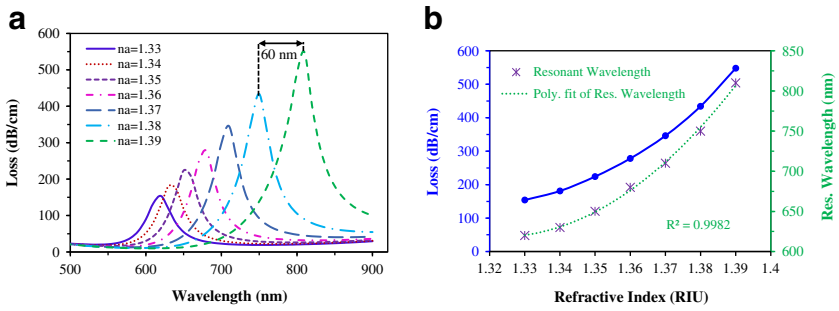

Fig. 4 **a** Fundamental loss spectrum and **b** linear fit of the resonant wavelength with varying analyte RI from 1.33 to 1.39 (with iteration of 0.01)

Real part in the effective refractive index of the SPP mode is strongly affected by the RI of analyte, resulting in the change of phase-matching wavelength with a small change in analyte RI. Figure 4a shows the effect of analyte RI on the loss spectrum. Increasing analyte RI will shift the SPP curve in Fig. 3a towards higher value collectively. This shifts the resonance peak loss towards longer wavelength. The increase in analyte RI also decreases the core-cladding index contrast which leads to higher light penetration to the cladding region. Hence, loss depth is increasing with the higher analyte RI. A minimum propagation loss of 154 dB/cm is achieved at n_a = 1.33 while the maximum propagation loss is 548 dB/cm at n_a = 1.39. A maximum resonance wavelength shift from 750 to 810 nm (60 nm) is found when the analyte RI is varied from 1.38 to 1.39. This allows the proposed sensor to have a maximum wavelength sensitivity of 6000 nm/RIU, which is higher than the reported PCF SPR sensors [15, 17, 18]. It also shows the sensor resolution of 1.67×10^{-5} RIU (by assuming minimum spectral resolution of 0.1 nm). Wavelength interrogation sensitivity is determined by the following Eq. 2;

$$S_\lambda(\lambda) = \frac{\Delta\lambda_{\text{peak}}}{\Delta n_a} \tag{2}$$

where $\Delta\lambda_{\text{peak}}$ is the peak shift and Δn_a is the variation in analyte RI. For the analyte RI of 1.33, 1.34, 1.35, 1.36, 1.37, and 1.38, the resonance loss peaks are found at the wavelength of 620, 630, 650, 680, 710, and 750 nm, respectively. This indicates that the wavelength sensitivities of 1000, 2000, 3000, 3000, and 4000 nm/RIU are achieved when the changes in analyte RI are 1.33–1.34, 1.34–1.35, 1.35–1.36, 1.36–1.37, and 1.37–1.38, respectively. Proposed sensor shows an average wavelength sensitivity of 3107 nm/RIU and the polynomial regression of resonant wavelength R^2 is 0.9987, which indicates the good fitting of the sensing performance (Fig. 4b). For the practical detection of analytes, self-calibration is needed with respect to RI range.

Compared to wavelength interrogation method, amplitude interrogation method is easier and cost effective since it requires measurement only at a specific wavelength [18].

Amplitude interrogation sensitivity is obtained from Eq. 3.

$$S_A(\lambda)\left[\text{RIU}^{-1}\right] = -\frac{1}{\alpha(\lambda, n_a)}\frac{\partial\alpha(\lambda, n_a)}{\partial n_a} \tag{3}$$

where $\partial\alpha(\lambda, n_a)$is the difference between two adjacent loss spectrum caused by the small change in analyte RI and ∂n_a and $\alpha(\lambda, n_a)$ are the overall loss. Increasing in analyte RI increases the amplitude sensitivity as shown in Fig. 5 due to the higher interaction between the evanescent field and SPP mode. The proposed sensor shows the maximum amplitude sensitivity of 508 RIU^{-1} at analyte RI of 1.38, which is comparable to reported works [14, 18], with simple sensor structure. Amplitude sensitivity of 120, 162, 204, 275, and 368 RIU^{-1} are demonstrated while the analyte RI's are 1.33, 1.34, 1.35, 1.36, and 1.37, respectively. It also shows the maximum sensor resolution of 1.97×10^{-5} RIU (considering amplitude sensitivity of 508 RIU^{-1}) by assuming minimum 1% change of transmitted intensity could be detected accurately.

Sensing performance of the proposed sensor is influenced by the thickness of gold layer because it has significant impact on the surface plasmon wave excitation. Figure 6 shows the variation of loss spectrum for analyte RI of 1.33 and 1.34 with varying gold thickness (other parameters are kept constant).

Using wavelength interrogation method, the proposed sensor shows the same sensitivity of 10 nm/RIU at the t_g of 50, 60, and 70 nm. However, the phase-matching wavelengths are

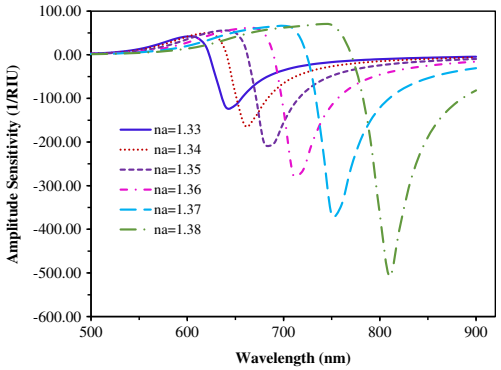

Fig. 5 Amplitude sensitivity spectrum for different analyte RI

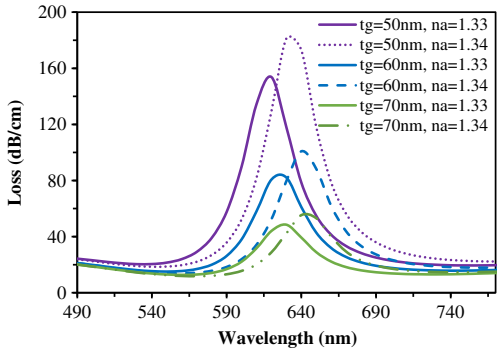

Fig. 6 Loss spectrums for different gold layer thickness

shifted towards the longer wavelength since the effective refractive index of SPP mode bound in gold layer is higher when t_g is increased. Thicker gold layer has more damping loss. Also, the loss depth is decreasing with the increasing of t_g because thicker gold layer reduce the penetration of core-guided mode into cladding. Considering the signal-to-noise ratio, gold thickness is chosen to be 50 nm for the proposed sensor.

Conclusion

In this work, we numerically investigated the DRF based SPR sensor, where the DRF is fabricated following the standard stack-and-draw fiber drawing method. The ease fabrication of DRF shows the feasibility to implement the DRF SPR sensor practically. DRF SPR sensor provides protected sensing medium with two large cavities where both cavities can be infiltrated by analyte. The proposed sensor shows an average wavelength sensitivity of 3107 nm/RIU, over the sensing RI range of 1.33–1.39. It demonstrates the maximum wavelength sensitivity of 6000 nm/RIU with the sensor resolution as high as 1.67×10^{-5} RIU. Additionally, maximum amplitude sensitivity is demonstrated to be 508 RIU^{-1} with resolution of 1.97×10^{-5} RIU. The results demonstrated the feasibility of DRF based SPR sensor towards an integrated SPR sensor as a lab-on-a-fiber technology for the real-time diagnostic purpose.

References

1. Homola J (2003) Present and future of surface plasmon resonance biosensors. Anal Bioanal Chem 377(3):528–539
2. Wong WR, Krupin O, Sekaran SD, Mahamd Adikan FR, Berini P (2014) Serological diagnosis of dengue infection in blood plasma using long-range surface plasmon waveguides. Anal Chem 86(3): 1735–1743
3. Rifat AA, Ahmed R, Yetisen AK, Butt H, Sabouri A, Mahdiraji GA, Yun SH, Adikan FM (2016) Photonic crystal fiber based plasmonic sensors. Sensors Actuators B Chem 243:311–325
4. Liedberg B, Nylander C, Lunström I (1983) Surface plasmon resonance for gas detection and biosensing. Sensors Actuators 4:299–304
5. Robinson G (1995) The commercial development of planar optical biosensors. Sensors Actuators B Chem 29(1):31–36
6. Rao Y, Zhu T A highly sensitive fiber-optic refractive index sensor based on an edge-written long-period fiber grating. In: Bragg Gratings, Photosensitivity, and Poling in Glass Waveguides, 2007. Optical Society of America, p JWA53
7. Zhao Y, X-g L, Cai L, Yang Y (2015) Refractive index sensing based on photonic crystal fiber interferometer structure with up-tapered joints. Sensors Actuators B Chem 221:406–410
8. Iadicicco A, Cusano A, Cutolo A, Bernini R, Giordano M (2004) Thinned fiber Bragg gratings as high sensitivity refractive index sensor. IEEE Photon Technol Lett 16(4):1149–1151
9. Ahmed R, Rifat AA, Yetisen AK, Yun SH, Khan S, Butt H (2016) Mode-multiplexed waveguide sensor. Journal of Electromagnetic Waves and Applications 30(4):444–455
10. Zhao Y, Cai L, Li X-G, Meng F-C, Zhao Z (2014) Investigation of the high sensitivity RI sensor based on SMS fiber structure. Sensors Actuators A Phys 205:186–190
11. Jorgenson R, Yee S (1993) A fiber-optic chemical sensor based on surface plasmon resonance. Sensors Actuators B Chem 12(3):213–220
12. Hassani A, Skorobogatiy M (2006) Design of the microstructured optical fiber-based surface plasmon resonance sensors with enhanced microfluidics. Opt Express 14(24):11616–11621
13. Shuai B, Xia L, Liu D (2012) Coexistence of positive and negative refractive index sensitivity in the liquid-core photonic crystal fiber based plasmonic sensor. Opt Express 20(23):25858–25866
14. Gao D, Guan C, Wen Y, Zhong X, Yuan L (2014) Multi-hole fiber based surface plasmon resonance sensor operated at near-infrared wavelengths. Opt Commun 313:94–98
15. Dash JN, Jha R (2014) SPR biosensor based on polymer PCF coated with conducting metal oxide. IEEE Photon Technol Lett 26(6): 595–598
16. Wang F, Sun Z, Liu C, Sun T, Chu PK (2016) A highly sensitive dual-core photonic crystal fiber based on a surface plasmon resonance biosensor with silver-graphene layer. Plasmonics:1–7
17. An G, Li S, Yan X, Zhang X, Yuan Z, Wang H, Zhang Y, Hao X, Shao Y, Han Z (2016) Extra-broad photonic crystal fiber refractive index sensor based on surface plasmon resonance. Plasmonics:1–7
18. Rifat A, Mahdiraji G, Chow D, Shee Y, Ahmed R, Adikan F (2015) Photonic crystal fiber-based surface plasmon resonance sensor with selective analyte channels and graphene-silver deposited core. Sensors 15(5):11499–11510
19. Dash JN, Jha R (2015) On the performance of graphene-based D-shaped photonic crystal fibre biosensor using surface plasmon resonance. Plasmonics 10(5):1123–1131
20. Tian M, Lu P, Chen L, Lv C, Liu D (2012) All-solid D-shaped photonic fiber sensor based on surface plasmon resonance. Opt Commun 285(6):1550–1554
21. Otupiri R, Akowuah E, Haxha S, Ademgil H, AbdelMalek F, Aggoun A (2014) A novel birefrigent photonic crystal fiber surface plasmon resonance biosensor. IEEE Photonics Journal 6(4):1–11
22. Rifat A, Mahdiraji GA, Sua Y, Shee Y, Ahmed R, Chow DM, Adikan FM (2015) Surface plasmon resonance photonic crystal fiber biosensor: a practical sensing approach. IEEE Photon Technol Lett 27(15):1628–1631
23. Hameed MFO, Alrayk YK, Shaalan AA, El Deeb WS, Obayya SS (2016) Design of highly sensitive multichannel bimetallic photonic crystal fiber biosensor. Journal of Nanophotonics 10(4):046016–046016
24. Hasan MR, Akter S, Rifat AA, Rana S, Ali S A highly sensitive gold-coated photonic crystal fiber biosensor based on surface

plasmon resonance. In: Photonics, 2017. vol 1. Multidisciplinary Digital Publishing Institute, p 18
25. Ng WL, Wong WR, Amouzad Mahdiraji G, Rifat AA, Tee DC, Mahamd Adikan FR (2017) Diamond ring fiber for evanescent field exposure. Opt Lett 42(8):1544–1547. doi:10.1364/OL.42.001544
26. Sazio PJ, Amezcua-Correa A, Finlayson CE, Hayes JR, Scheidemantel TJ, Baril NF, Jackson BR, Won D-J, Zhang F, Margine ER (2006) Microstructured optical fibers as high-pressure microfluidic reactors. Science 311(5767):1583–1586
27. Boehm J, François A, Ebendorff-Heidepriem H, Monro TM (2011) Chemical deposition of silver for the fabrication of surface plasmon microstructured optical fibre sensors. Plasmonics 6(1):133–136
28. Wu C, Tse M-LV, Liu Z, Guan B-O, Lu C, Tam H-Y (2013) In-line microfluidic refractometer based on C-shaped fiber assisted photonic crystal fiber Sagnac interferometer. Opt Lett 38(17):3283–3286
29. Tatian B (1984) Fitting refractive-index data with the Sellmeier dispersion formula. Appl Opt 23(24):4477–4485. doi:10.1364/AO.23.004477
30. Vial A, Grimault A-S, Macías D, Barchiesi D, de la Chapelle ML (2005) Improved analytical fit of gold dispersion: application to the modeling of extinction spectra with a finite-difference time-domain method. Phys Rev B 71(8):085416
31. Amouzad Mahdiraji G, Chow DM, Sandoghchi SR, Amirkhan F, Dermosesian E, Yeo KS, Kakaei Z, Ghomeishi M, Poh SY, Yu Gang S, Mahamd Adikan FR (2014) Challenges and solutions in fabrication of silica-based photonic crystal fibers: an experimental study. Fiber and Integrated Optics 33(1–2):85–104. doi:10.1080/01468030.2013.879680